Supplementary Information (SI) for Inorganic Chemistry Frontiers.
This journal is © the Partner Organisations 2026

Supporting Information

New members of the lanthanide titanium cluster family: Janus nanoclusters, and their optical imaging and photodynamic therapy

Ru-Yan Li,[a,+] Wen-Wen Qin,[b,+] Fan Yang,[b,+] Hai-Ling Wang,[a,] Meng-Juan Tang,[b] Hua-Hong Zou,[b,*] Fu-Pei Liang,[b,*] De-Xin Chen,[a] Zhong-Hong Zhu[a]*

[a]*School of Chemistry and Chemical Engineering, Guangxi Key Laboratory of Electrochemical Energy Materials, Guangxi University, Nanning, 530004, P. R. China.*

[b]*Key Laboratory for Chemistry and Molecular Engineering of Medicinal Resources (Ministry of Education of China), Guangxi Key Laboratory of Chemistry and Molecular Engineering of Medicinal Resources, School of Chemistry and Pharmaceutical Sciences, Guangxi Normal University, Guilin 541004, P. R. China*

**E-mail: gxnuchem@foxmail.com (H.-H. Zou), liangfupei@glut.edu.cn (F.-P. Liang), and whling@gxu.edu.cn (H.-L. Wang).*

Keywords: Lanthanide cluster; assembly mechanism; lanthanide luminescence; optical imaging; photodynamic therapy

Table of Contents:

Figure S13	TDOS and PDOS of individual atoms for Gd_4Ti_{14} (the position of the Fermi level is indicated by a red dashed line at 0 eV).
Figure S14	(A) ROS detection mechanism of DCFH; (B) Changes in the PL spectrum of DCFH under light irradiation (60 mW/cm^2); (C) Changes in the PL spectrum of DCFH under light irradiation (60 mW/cm^2) in the presence of Gd_4Ti_{14}; (D) ROS generation of Gd_4Ti_{14} under white light irradiation (60 mW/cm^2) observed by DCFH fluorescence enhancement technology.
Figure S15	(A) $\cdot O_2^-$ detection mechanism of DHR 123; (B) Changes in the PL spectrum of DHR 123 under illumination (60 mW/cm^2); (C) Changes in the PL spectrum of DHR 123 under illumination (60 mW/cm^2) in the presence of Gd_4Ti_{14}; (D) Monitoring the $\cdot O_2^-$ generation ability of Gd_4Ti_{14} under illumination conditions (60 mW/cm^2) using DHR 123.
Figure S16	(A) $^1O_2$ detection mechanism of ABDA; (B) UV-vis absorption spectra of ABDA after irradiation at different times (60 mW/cm^2); (C) The absorption spectrum of ABDA changes under different irradiation times (60 mW/cm^2) in the presence of Gd_4Ti_{14}; (D and E) The $^1O_2$ generation ability of Gd_4Ti_{14} under light conditions (60 mW/cm^2) was monitored using ABDA.
Figure S17	Inhibitory effects of different concentrations of Eu_4Ti_{14} on the growth of (A) HeLa, (B) MDA-MB-231 and (C) 4T1 cells.
Figure S18	(A) CLSM images and quantitative analysis of fluorescence intensity after co-incubation of Eu_4Ti_{14} with WI-38 cells; (B) CLSM images of Eu_4Ti_{14} and LysoTracker Green in lysosomes of HeLa cells, respectively; quantitative analysis of fluorescence intensity of Eu_4Ti_{14} and LysoTracker Green in HeLa cells.
Figure S19	(A and B) CLSM images of Zebrafish embryos co-incubated with Eu_4Ti_{14} for 1, 2, 3, 6, and 12 h; (C) CLSM images of Zebrafish larvae co-incubated with Eu_4Ti_{14} for 1, 2, 3, 6, and 12 h; (D) Quantitative analysis of fluorescence intensity of Zebrafish larvae co-incubated with Eu_4Ti_{14} for 1, 2, 3, 6, and 12 h.
Figure S20	DLS results and Zeta potential of Gd_4Ti_{14}.
Figure S21	JC-1 staining was used to monitor the changes of mitochondrial membrane

	potential in different experimental groups.
Figure S22	Healthy mice were intravenously injected with PBS or Gd_4Ti_{14} (100 μg/mL, 50 μL) for 24 hours before routine blood analysis (data are expressed as mean ± SD, n = 3, no significant differences).
Figure S23	H&E staining results of important organ sections of healthy mice intravenously injected with PBS or Gd_4Ti_{14} (100 μg/mL, 50 μL).

Experimental

Materials and Measurements

All reagents were purchased from commercial sources and used without further purification. Elemental analyses of C, H, O, N, and Eu/Gd were performed using a Varia MICRO cube. Infrared spectra were recorded using a PE Spectrum FT-IR spectrometer (400-4000 cm^{-1}) with approximately 0.5% KBr. Thermogravimetric analysis (TGA) was performed under a nitrogen flow at a heating rate of 5 °C/min using a NETZSCH TG 209 F3 instrument. Powder X-ray diffraction (PXRD) spectra were recorded at 298 K (Mo-Kα) using a Bruker SMART CCD diffractometer. UV-visible absorption spectra were recorded using a Shimadzu UV-2600 spectrophotometer. EPR spectra of Gd_4Ti_{14} were obtained using a Bruker A300 instrument. Transmission electron microscopy (TEM) images and energy-dispersive spectroscopy (EDS) elemental mapping were recorded using a ThermoFisher Scientific Talos F200S transmission electron microscope. The absorbance intensity of 3-(4,5-dimethylthiazol-2-yl)-2,5-diphenyltetrazolium bromide (MTT) was measured using a Cytation 5 Multifunctional Detection System. Cell imaging, zebrafish imaging, and colocalization were recorded using a TCS SPB DIVE two-photon laser confocal microscope. Flow cytometry was performed using a BD LSRFortessa X-20 flow cytometer.

The Synthesis Method

Synthesis of $[Eu_4Ti_{14}(L)_{24}(\mu_3\text{-}O)_{19}(\mu_2\text{-}O)_3(C_3H_8O)(H_2O)_2]\cdot(C_7H_6O_2)_2\cdot(CH_3CN)_3$

In a 25 mL reactor, add 0.2 mmol $Eu(NO_3)_3\cdot 6H_2O$, 0.6 mmol isopropyl titanate, 7.5 mmol benzoic acid, and a mixed solvent (IPA:CH_3CN = 1:3). Stir for 30 min. Place the reactor in an oven at 100 °C for 34 h. Remove the reaction vessel and slowly cool it to room temperature to precipitate colorless block

crystals. Elemental analysis theoretical value ($C_{191}H_{151}Eu_4N_3O_{77}Ti_{14}$): C, 45.89%; H, 3.04%; N, 0.84%; experimental value: C, 45.70%; H, 3.25%; N, 1.07%; Infrared spectral data (IR, KBr, cm^{-1}): 3443(s), 2363(w), 1598(m), 1547(m), 1420(s), 1177(w), 717(m), 653(w).

Synthesis of $[Gd_4Ti_{14}(L)_{24}(\mu_3\text{-}O)_{19}(\mu_2\text{-}O)_3(C_3H_8O)(H_2O)_2]\cdot(C_7H_6O_2)_2\cdot(CH_3CN)_3$

The synthesis steps are similar to those for Eu_4Ti_{14}, except that $Eu(NO_3)_3\cdot6H_2O$ is replaced with $Gd(NO_3)_3\cdot6H_2O$. Elemental analysis theoretical value ($C_{191}H_{151}Gd_4N_3O_{77}Ti_{14}$): C, 45.70%; H, 3.03%; N, 0.84%; experimental value: C, 44.96%; H, 3.15%; N, 0.86%; Infrared spectral data (IR, KBr, cm^{-1}): 3063 (w), 2353 (w), 1597 (m), 1550 (m), 1417 (s), 1176 (w), 1069 (w), 717 (m), 655 (w).

Single-crystal X-ray crystallography

Diffraction data for the complex was collected on a Bruker SMART CCD diffractometer (Cu-K_α radiation and λ = 1.54 Å) in Φ and ω scan modes. The structures were solved by direct methods, followed by difference Fourier syntheses, and then refined by full-matrix least-squares techniques on F^2 using *SHELXL*. All other non-hydrogen atoms were refined with anisotropic thermal parameters. Hydrogen atoms were placed at calculated positions and isotopically refined using a riding model. Table S1 summarizes X-ray crystallographic data and refinement details for the complex. The CCDC reference number for the crystal structure of Gd_4Ti_{14} is 2486699.

HRESI-MS measurements

HRESI-MS measurements were performed at a capillary temperature of 275 °C. A 2 mL aliquot of the solution was injected into the apparatus. The mass spectrometer used for the measurements was a

ThermoExactive, and data were collected in positive ion mode. The spectrometer was previously calibrated with a standard tuning mixture, providing an accuracy of approximately 2 ppm over the *m*/*z* range of 200~4000. The capillary voltage was 50 V, the tube lens voltage was 150 V, and the skimmer voltage was 25 V.

Total ROS detection

After activation, 2',7'-dichlorodihydrofluorescein diacetate (DCFH-DA) is converted into DCFH, which is used for the detection of total ROS. The specific steps are as follows: 20 μL of Gd_4Ti_{14} solution (1 mM, dissolved in DMSO) was added to 1980 μL of DCFH (50 μM) aqueous solution. After the above solution is irradiated with a xenon lamp white light (60 mW/cm^2) for different periods, the change in the fluorescence signal of the indicator is monitored by a fluorescence spectrometer. The excitation wavelength is 480 nm, and the fluorescence intensity of DCFH at 525 nm is recorded to indicate ROS generation.

Superoxide anion radical ($\cdot O_2^-$) detection

Dihydrorhodamine 123 (DHR 123) was used as an indicator of $\cdot O_2^-$. The specific steps are as follows: 20 μL of Gd_4Ti_{14} solution (1 mM, dissolved in DMSO) was added to 1980 μL of DHR 123 (50 μM) aqueous solution. After irradiating the solution with white light by a xenon lamp of 60 mW/cm^2 for predesignated time, the change in the fluorescence signal of the indicator is monitored by a fluorescence spectrometer. The excitation wavelength used is 480 nm, and the fluorescence intensity of DHR 123 at 525 nm is recorded to indicate $\cdot O_2^-$ generation.

Singlet oxygen ($^1O_2$) detection of ABDA

9,10-Anthracenediyl-bis(methylene)-dimalonic acid (ABDA) was used to monitor $^1O_2$ production. The specific steps are as follows: 20 μL of Gd_4Ti_{14} solution (1 mM, dissolved in DMSO) was added to 1980 μL of ABDA (50 μM) aqueous solution. After irradiating the solution with white light by a xenon lamp of 60 mW/cm^2 for predesignated time, the change in the absorption signal of the indicator ABDA at 380 nm was monitored by an ultraviolet-visible spectrometer to monitor the generation of $^1O_2$.

ROS detection with electron paramagnetic resonance (EPR)

DMPO was used as a trapping agent for·O_2^-. TEMP was used as the trapping agent for $^1O_2$. Gd_4Ti_{14} was dispersed in DMSO, and DMPO/TEMP was dissolved in CH_3OH. The trapping agent solution was then added to the Gd_4Ti_{14} solution. Electron paramagnetic resonance (EPR) spectra of the mixture were recorded before and after illumination (xenon lamp, 3 min for DMPO, 2 min for TEMP, 60 mW/cm^2).

MTT assay of Eu_4Ti_{14}

The MTT assay was used to investigate the cytotoxicity of Eu_4Ti_{14} against HeLa, MDA-MB-231, and 4T1 cells. Cells were grown adherently in an incubator at 37 °C and 5% CO_2. Cells were incubated with various concentrations of Eu_4Ti_{14}. Cell viability was calculated based on MTT absorbance.

Cells imaging of Eu_4Ti_{14}

HeLa, MDA-MB-231, 4T1, and WI-38 cells were cultured in 20 mm glass-bottomed culture dishes at 37 °C in a humidified atmosphere with 5% CO_2. After cell growth reached 90%, the cells were washed

three times with PBS. A 20 mg/mL Eu_4Ti_{14} solution (final concentration 25 μg/mL) was then added to the culture dishes. After 12 h of incubation, the dishes were removed, washed three times with PBS, and CLSM images were acquired.

Zebrafish imaging of Eu_4Ti_{14}

Unhatched embryos and Zebrafish larvae were placed in 20 mm glass-bottomed culture dishes and incubated at room temperature. Eu_4Ti_{14} solution was then added to the dishes to a final concentration of 25 μg/mL. After incubation for 1, 2, 3, 6, and 12 h, the embryos and larvae were washed three times, and CLSM images were acquired.

Intracellular ROS detection

Gd_4Ti_{14} labeled 4T1 cells were incubated with ROS indicator 2',7'-dichlorodihydrofluorescein diacetate (DCFH-DA) for 30 min, followed by white light (60 mW/cm^2) exposure for 10 min. The cells were then imaged by CLSM with an excitation filter of 488 nm and an emission filter of 500-530 nm. Dihydroethidium (DHE) fluorescence probe was further used to detect the $\cdot O_2^-$ level in cells. The Gd_4Ti_{14} labeled 4T1 cells were incubated with a DHE fluorescence probe for 30 min, followed by white light (60 mW/cm^2) exposure for 10 min. After washing with PBS, the cells were observed by CLSM. The red fluorescence from DHE was collected from 600 to 630 nm upon excitation at 532 nm.

Live/dead cell staining

4T1 cells were seeded into laser confocal petri dishes at a density of 2 × 10^5 cells/dish. After incubating cells with sample for 6 h and subjecting them to various treatments (with/without 60

mW/cm^2 white light irradiation for 10 min), 4T1 cells were incubated with a mixture of calcein acetoxymethyl ester (CAM) (2 μg/mL) and propidium iodide (PI) (5 μg/mL). After washing with PBS, the cells were observed by CLSM. The green fluorescence from CAM was collected from 500 to 530 nm upon excitation at 488 nm, and the red fluorescence from PI was collected from 600 to 630 nm upon excitation at 532 nm.

Flow cytometry analysis

4T1 cells were seeded on 6-well plates at a density of 2 × 10^5 cells/well and cultured overnight for cell adherence. Four different experimental groups (PBS, PBS+L, Gd_4Ti_{14} (50 μg/mL), and Gd_4Ti_{14} (50 μg/mL)+L) were set up, and 4T1 cells treated in the above experimental groups were further incubated for 12 h, and then cells were rinsed with PBS and trypsinzed. Cells were then collected by centrifugation and resuspending in PBS and then incubated with the mixture of Annexin V-FITC and PI in the dark for 10 min. After rinsed with PBS, all samples were measured with a BD LSRFortessa X-20 flow cytometer using a 488 nm laser for Annexin V-FITC and a 561 nm laser for PI excitation.

Construction of tumor models

All mice were kept in SPF-level feeding conditions with adequate water and food. The temperature is kept at 26 °C, the humidity is 50 %, and a 12 h light/dark cycle. Female mice (BALB/c, 6-8 weeks old) were inoculated subcutaneously with mouse breast cancer cells, i.e., 50 μL 4T1 cells (2 × 10^6) suspensions were injected subcutaneously into the right limb of the mice to obtain a tumor-bearing mice model. When tumors reached an average volume of 150 mm^3, mice were used to evaluate the effectiveness of different treatments (Volume = length*width*width /2). All animal procedures were

approved by the Institutional Animal Care and Use Committee (IACUC) of the Guangxi Normal University (accreditation number: No.202509-002).

***In vivo* PDT assay**

The tumor-bearing mice were randomly divided into four groups, including PBS, PBS+L, Gd_4Ti_{14}, and Gd_4Ti_{14}+L groups. 50 μL PBS was injected intratumorally into the tumors of each mouse in PBS and PBS+L groups. 50 μL Gd_4Ti_{14} (100 μg/mL) was injected intratumorally into the tumors of each mouse in Gd_4Ti_{14} and Gd_4Ti_{14}+L groups. After 1 h, the mice in PBS+L, and Gd_4Ti_{14}+L groups were irradiated with white light of 60 mW/cm^2 for 15 min, while PBS and Gd_4Ti_{14} groups were not irradiated. Tumor size and mice weight were recorded every other day for 12 days. At day 12 post-treatment, the mice were sacrificed, and the heart, liver, spleen, lung, and kidney organs were extracted and fixed with 4% paraformaldehyde for H&E staining to determine whether Gd_4Ti_{14} caused organ damage. In addition, Gd_4Ti_{14} (100 μg/mL, 50 μL) was injected into the healthy mice without tumors through the tail vein, and the PBS group was used as the control group. 24 h after injection, blood samples were collected from mice for detection of hematological markers. Through the detection and analysis of blood parameters such as red blood cells, white blood cells, and platelets, to determine whether there are infection, anemia, bleeding, and other abnormalities in mice after injection of Gd_4Ti_{14} through the tail vein to prove the biological safety of Gd_4Ti_{14}. The fixed tissues were processed into paraffin, sliced at a thickness of 5 mm for hematoxylin and eosin (H&E), and TdT-mediated dUTP Nick-End Labeling (TUNEL) staining and the morphology of tumor tissues was observed by using an OLYMPUS BX51-PMS microscope.

Statistical Analysis

Data between two groups were analyzed by an independent *t* test, and more than two groups were tested by one-way ANOVA followed by a suitable post-hoc analysis. For all tests, $P < 0.05$ was considered statistically significant. Data were expressed as the mean ± SD (standard deviation).

Table S1. Crystallographic data of Gd_4Ti_{14}.

Cluster	**Gd_4Ti_{14}**
Formula	$C_{191}H_{151}Gd_4N_3O_{77}Ti_{14}$
Formula weight	5019.328
T (K)	100
Crystal system	triclinic
Space group	P-1
a (Å)	18.1942(2)
b (Å)	18.9480(2)
c (Å)	32.5191(3)
α (°)	89.891(1)
β (°)	77.613(1)
γ (°)	67.831(1)
V (Å^3)	10101.5(2)
Z	2
D_c (g cm^{-3})	1.637
μ (mm^{-1})	13.53
Reflns coll.	185769
Unique reflns	40807
R_{int}	0.153
$^aR_1[I \geq 2\sigma(I)]$	0.106
$^bwR_2$(all data)	0.289
GOF	1.056

$^aR_1=\Sigma||F_o|-|F_c||/\Sigma|F_o|$, $^bwR_2 = \Sigma[w(F_o^2-F_c^2)^2]/\Sigma[w(F_o^2)^2]^{1/2}$

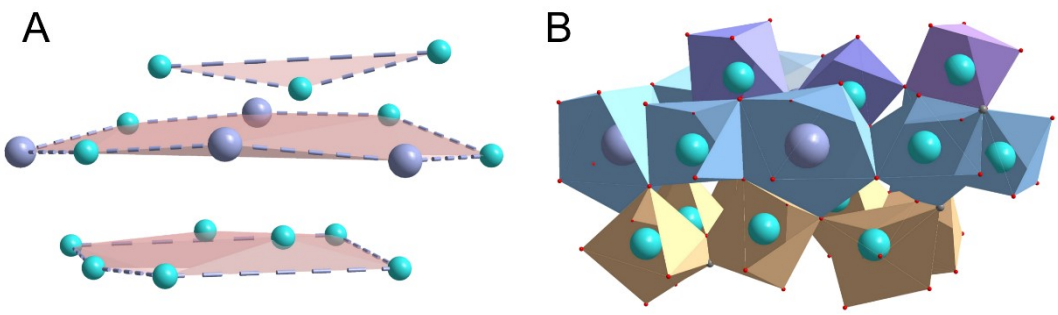

Figure S1. (A) Disassembled diagram of the metal cluster core of Ln_4Ti_{14}; (B) Polyhedron diagram of the metal cluster core of Ln_4Ti_{14}.

Table S2. Cluster core structure statistics of lanthanide-titanium clusters.

Numbers	Cluster core structure	Molecular formula	Journals published
1	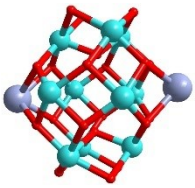	Ln_2Ti_{10}	*Dalt. Trans.* **2015**, *44* (4), 1882-1888.
2	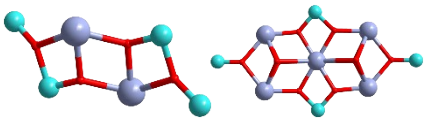	Eu_2Ti_4 Eu_5Ti_4	*Inorg. Chem.* **2017**, *56* (20), 12186-12192.
3	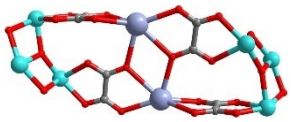	Ln_2Ti_6	*New J. Chem.* **2018**, *42* (14), 11629-11634.
4	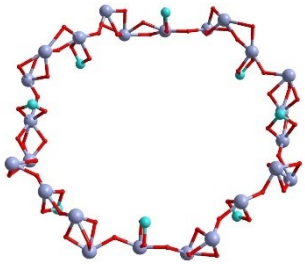	$Eu_{24}Ti_8$	*Angew. Chem. Int. Ed.* **2018**, *57* (34), 10976-10979.
5	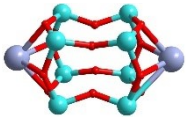	Ln_2Ti_8	*Inorg. Chem.* **2019**, *58* (22), 15008-15012.

6	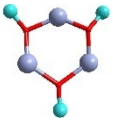	Eu_3Ti_3	*Inorg. Chem.* **2019**, *58* (15), 10078-10083.
7	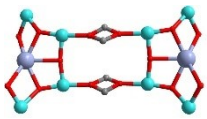	Ln_2Ti_8	*J. Mol. Liq.* **2020**, *317*, 113946.
8	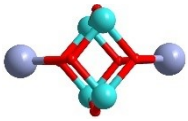	Eu_2Ti_4	*Inorg. Chem.* **2020**, *59* (17), 12404-12409.
9	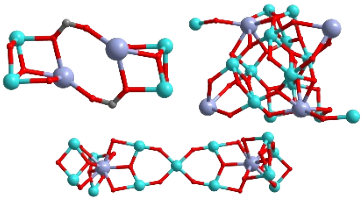	Gd_2Ti_4 Gd_2Ti_{13} Gd_4Ti_{14}	*Inorg. Chim. Acta* **2021**, *528* (5), 120621.
10	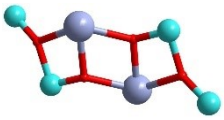	Eu_2Ti_4	*Chem. Commun.* **2022**, *59* (3), 346-349.
11	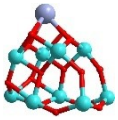	$LnTi_9$	*Inorg. Chem. Commun.* **2022**, *141* (5), 109565.
12		Ln_9Ti_2	*Inorg. Chem.* **2022**, *61* (26), 98499854.
13	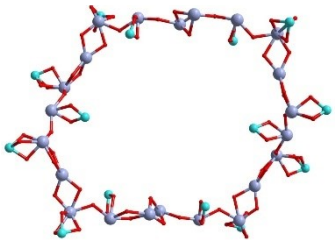	$Ln_{22}Ti_{14}$	*Angew. Chem. Int. Ed.* **2022**, *61* (8), e202116296.
14	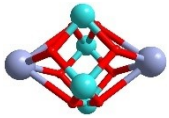	Eu_2Ti_4	*Sci. China Chem.* **2024**, *67* (2), 529-535.
15	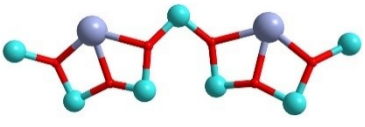	Ln_2Ti_7	*Inorg. Chem. Front.* **2025**, *12* (1), 253-260.

16	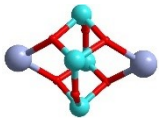	Eu_2Ti_4	*J. Rare Earths* **2025**, *43* (8), 1590-1600.
17	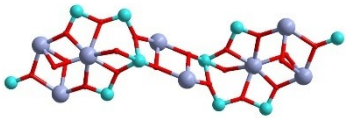	Eu_8Ti_{10}	*Nano Lett.* **2025**, *25* (3), 1199-1206.
18	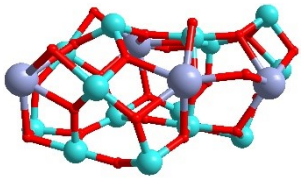	**Ln_4Ti_{14}**	**This work**

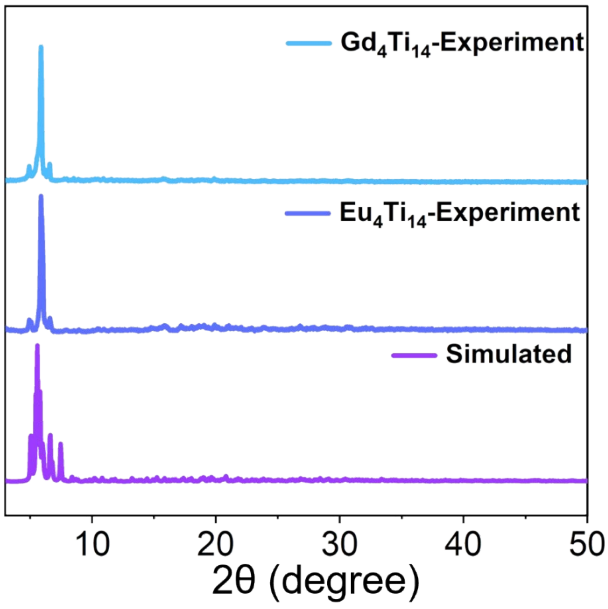

Figure S2. Powder X-ray diffraction (PXRD) pattern of Ln_4Ti_{14}.

FT-IR analysis

Eu_4Ti_{14} and Gd_4Ti_{14} are isostructural and exhibit identical Fourier transform infrared (FT-IR) characteristic absorption peaks at the same positions (Figure S3). The broad, intense absorption peak near 3440 cm^{-1} in the IR spectrum is attributed to the v(HO-H) vibration of the H_2O molecule; the peak near 1600 cm^{-1} is attributed to the stretching vibration of the C=C bond in the benzene ring; the

strong peak near 1420 cm^{-1} is attributed to the stretching vibration of the C-O bond in the carboxylic acid; and the moderately strong peak near 720 cm^{-1} is attributed to the out-of-plane bending vibration of the C-H bond in the benzene ring.

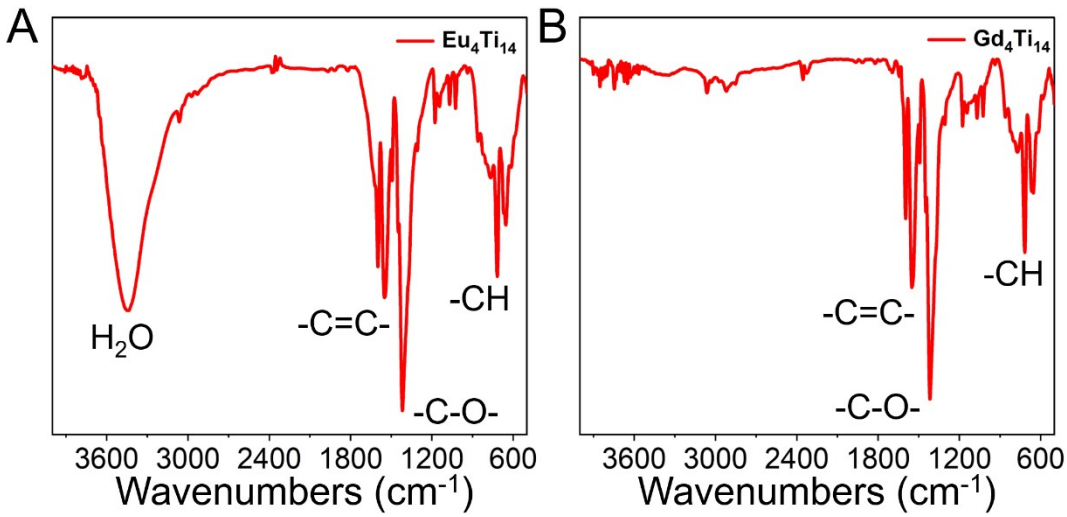

Figure S3. FT-IR spectrum of Ln_4Ti_{14}.

TG analysis

The thermal stability of Eu_4Ti_{14} and Gd_4Ti_{14} was tested under a flowing nitrogen atmosphere. The temperature was slowly increased from 35 °C to 1000 °C at a rate of 5 °C/min. Eu_4Ti_{14} decomposed at 300 °C (Figure S4A). The weight loss of Eu_4Ti_{14} was 2.5%, corresponding to the loss of three free CH_3CN solvent molecules (theoretical value: 2.46%). Gd_4Ti_{14} decomposed at 330 °C (Figure S4B). The weight loss of Gd_4Ti_{14} was 3.02%, corresponding to the loss of three free CH_3CN solvent molecules and two terminally coordinated H_2O molecules (theoretical value: 3.16%). Both Eu_4Ti_{14} and Gd_4Ti_{14} decomposed as the temperature continued to increase.

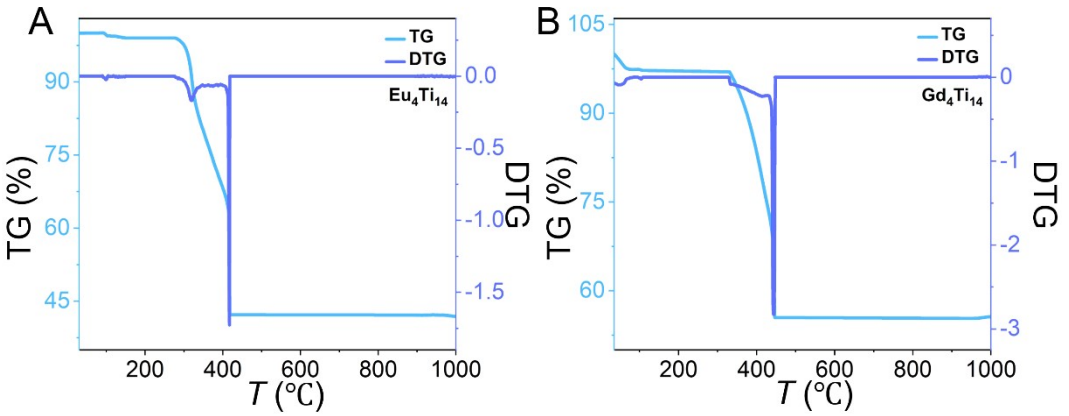

Figure S4. TG and DTG curves of Ln_4Ti_{14}.

Table S3. Major species assigned in the HRESI-MS of Eu_4Ti_{14} in positive mode.

Numbers	Fragments	*Exp. m/z*	*Cal. m/z*
1	$[Eu_4Ti_{14}(L)_{17}(\mu_3\text{-}O)_{19}(\mu_2\text{-}O)_3(OH)_5(CH_3CN)(C_3H_8O)_2(H_2O)_2]^{2+}$	1985.72	1985.76
2	$[Eu_4Ti_{14}(L)_{18}(\mu_3\text{-}O)_{19}(\mu_2\text{-}O)_3(OH)_4(C_3H_8O)_2(CH_3OH)(H_2O)H]^{2+}$	2024.72	2024.77
3	$[Eu_4Ti_{14}(L)_{18}(\mu_3\text{-}O)_{19}(\mu_2\text{-}O)_3(OH)_4(C_3H_8O)(CH_3CN)_2(H_2O)_3]^{2+}$	2037.22	2037.26
4	$[Eu_4Ti_{14}(L)_{18}(\mu_3\text{-}O)_{19}(\mu_2\text{-}O)_3(OH)_4(C_3H_8O)(CH_3CN)_4(CH_3OH)(H_2O)]^{2+}$	2076.24	2076.29
5	$[Eu_4Ti_{14}(L)_{19}(\mu_3\text{-}O)_{19}(\mu_2\text{-}O)_3(OH)_3(C_3H_8O)_3(CH_3CN)_2(H_2O)_5]^{2+}$	2167.39	2167.34
6	$[Eu_4Ti_{14}(L)_{20}(\mu_3\text{-}O)_{19}(\mu_2\text{-}O)_3(OH)_2(C_3H_8O)(CH_3CN)_3(H_2O)_8]^{2+}$	2206.89	2206.83

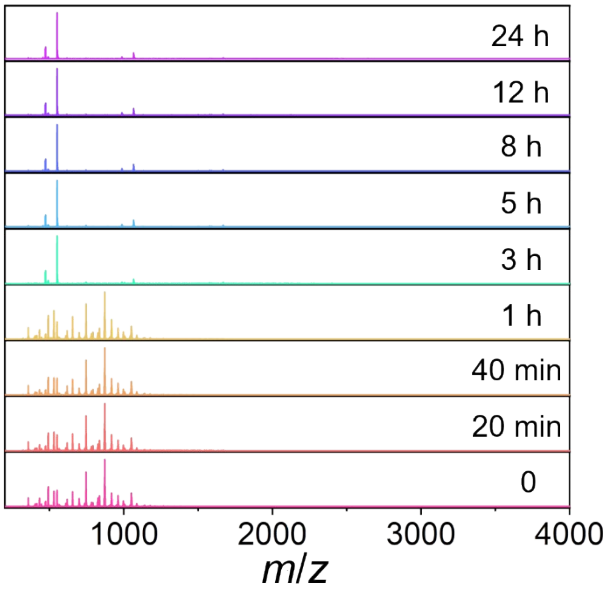

Figure S5. Time-dependent HRESI-MS spectra of Eu_4Ti_{14} in the range of *m/z* = 200~4000.

Table S4. Major species assigned in the time-dependent HRESI-MS for tracked the formation of Eu_4Ti_{14} in positive mode.

Fragments	***Exp. m/z***	***Cal. m/z***
$[EuTi(L)_3(OH)_2(C_3H_8O)_3(DMSO)_2(CH_3OH)(H_2O)]^{2+}$	491.96	492.09
$[EuTi(L)_2(OH)_4(H_2O)]^{+}$	529.01	528.95
$[EuTi(L)_3(OH)_2(DMSO)_5(CH_3OH)_3(H_2O)]^{2+}$	551.00	551.05
$[Ti_2(L)_2(\mu_2\text{-}O)(OH)_3(CH_3CN)_4(CH_3OH)(H_2O)_3]^{+}$	655.00	655.12
$[Ti_2(L)_2(\mu_2\text{-}O)(OH)_3(DMSO)_3(C_3H_8O)]^{+}$	698.96	699.05
$[Ti_2(L)_3(\mu_2\text{-}O)(OH)_2(CH_3CN)_4(H_2O)_4]^{+}$	745.01	745.13
$[Ti_2(L)_3(\mu_2\text{-}O)(OH)_2(DMSO)_4(CH_3OH)(H_2O)]^{+}$	870.99	871.07
$[EuTi_3(L)_5(\mu_3\text{-}O)(\mu_2\text{-}O)_3(OH)(C_3H_8O)(CH_3OH)_3HH]^{+}$	1141.01	1141.04
$[EuTi_3(L)_5(\mu_3\text{-}O)(\mu_2\text{-}O)_3(OH)(CH_3OH)(H_2O)_9]^{+}$	1176.98	1177.01

$[EuTi_3(L)_6(\mu_3\text{-}O)(\mu_2\text{-}O)_3(C_3H_8O)_3]^+$	1266.99	1267.09
$[EuTi_5(L)_7(\mu_3\text{-}O)_4(\mu_2\text{-}O)(OH)_5(C_3H_8O)(CH_3OH)_3(H_2O)]^+$	1578.84	1579.00
$[EuTi_5(L)_8(\mu_3\text{-}O)_4(\mu_2\text{-}O)(OH)_4(C_3H_8O)(CH_3CN)_2(H_2O)]^+$	1668.85	1669.00
$[Eu_2Ti_6(L)_8(\mu_3\text{-}O)_5(\mu_2\text{-}O)_4(OH)_3H_4]^+$	1758.87	1758.76
$[Eu_3Ti_{11}(L)_{18}(\mu_3\text{-}O)_{13}(\mu_2\text{-}O)_3(OH)(CH_3CN)_4(H_2O)_6]^{2+}$	1853.75	1853.90
$[Eu_3Ti_{11}(L)_{18}(\mu_3\text{-}O)_{13}(\mu_2\text{-}O)_3(OH)(C_3H_8O)(H_2O)_7(CH_3CN)_4]^{2+}$	1892.77	1892.93
$[Eu_3Ti_{11}(L)_{18}(\mu_3\text{-}O)_{13}(\mu_2\text{-}O)_3(OH)(C_3H_8O)_7(CH_3OH)(H_2O)_3]^{2+}$	1970.78	1971.05
$[Eu_4Ti_{14}(L)_{20}(\mu_3\text{-}O)_{19}(\mu_2\text{-}O)_3(OH)_2(C_3H_8O)_2(CH_3CN)]^{2+}$	2123.78	2123.79
$[Eu_4Ti_{14}(L)_{24}(\mu_3\text{-}O)_{19}(\mu_2\text{-}O)_3(C_6H_5CO)_2(CH_3OH)(H_2O)H]^{2+}$	2398.81	2398.89

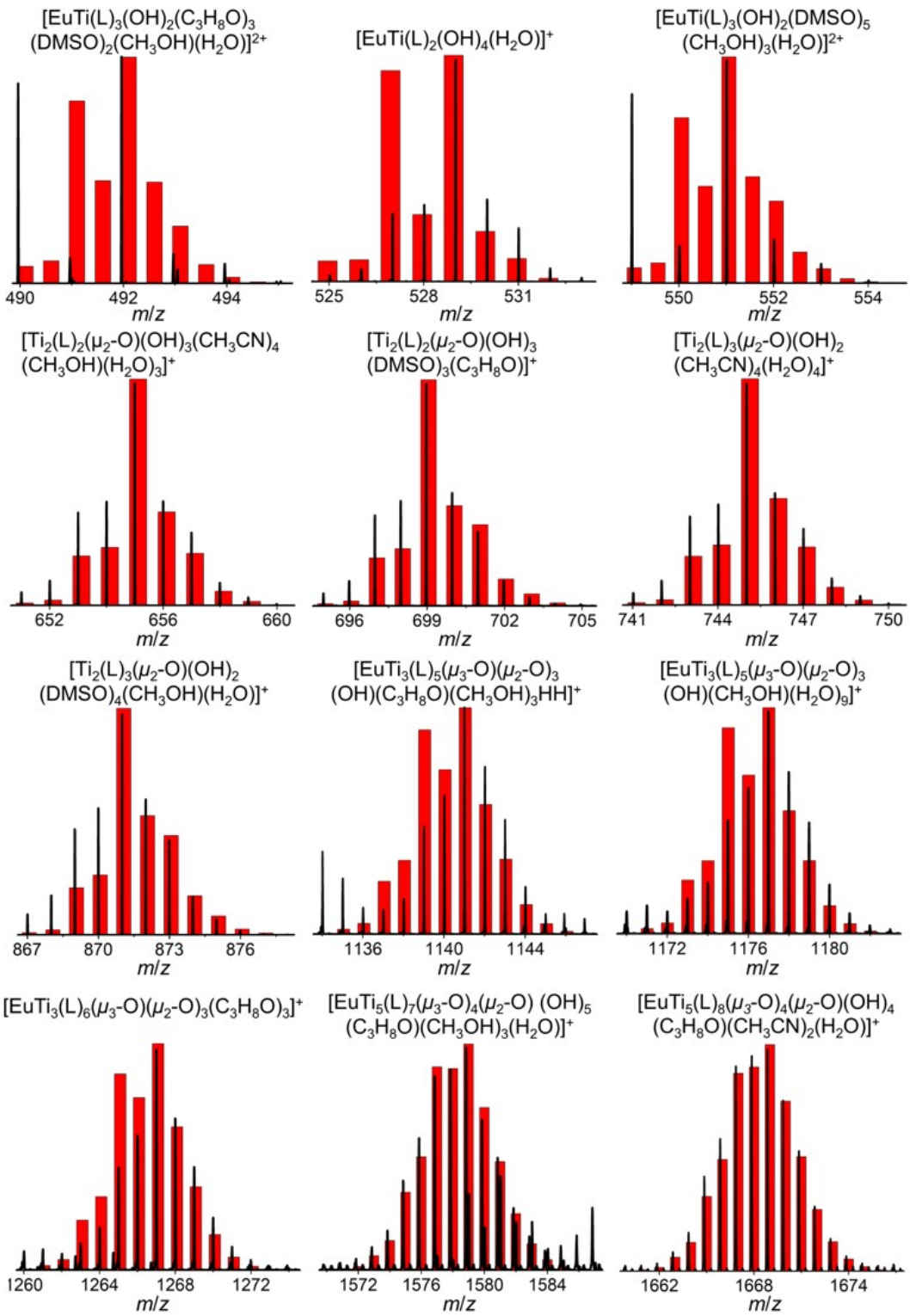
[EuTi(L)3(OH)2(C3H8O)3 (DMSO)2(CH3OH)(H2O)]2+
490
492
494
m/z
[EuTi(L)2(OH)4(H2O)]+
525
528
531
m/z
[EuTi(L)3(OH)2(DMSO)5 (CH3OH)3(H2O)]2+
550
552
554
m/z
[Ti2(L)2(μ2-O)(OH)3(CH3CN)4 (CH3OH)(H2O)3]+
652
656
660
m/z
[Ti2(L)2(μ2-O)(OH)3 (DMSO)3(C3H8O)]+
696
699
702
705
m/z
[Ti2(L)3(μ2-O)(OH)2 (CH3CN)4(H2O)4]+
741
744
747
750
m/z
[Ti2(L)3(μ2-O)(OH)2 (DMSO)4(CH3OH)(H2O)]+
867
870
873
876
m/z
[EuTi3(L)5(μ3-O)(μ2-O)3 (OH)(C3H8O)(CH3OH)3HH]+
1136
1140
1144
m/z
[EuTi3(L)5(μ3-O)(μ2-O)3 (OH)(CH3OH)(H2O)9]+
1172
1176
1180
m/z
[EuTi3(L)6(μ3-O)(μ2-O)3(C3H8O)3]+
1260
1264
1268
1272
m/z
[EuTi5(L)7(μ3-O)4(μ2-O) (OH)5 (C3H8O)(CH3OH)3(H2O)]+
1572
1576
1580
1584
m/z
[EuTi5(L)8(μ3-O)4(μ2-O)(OH)4 (C3H8O)(CH3CN)2(H2O)]+
1662
1668
1674
m/z

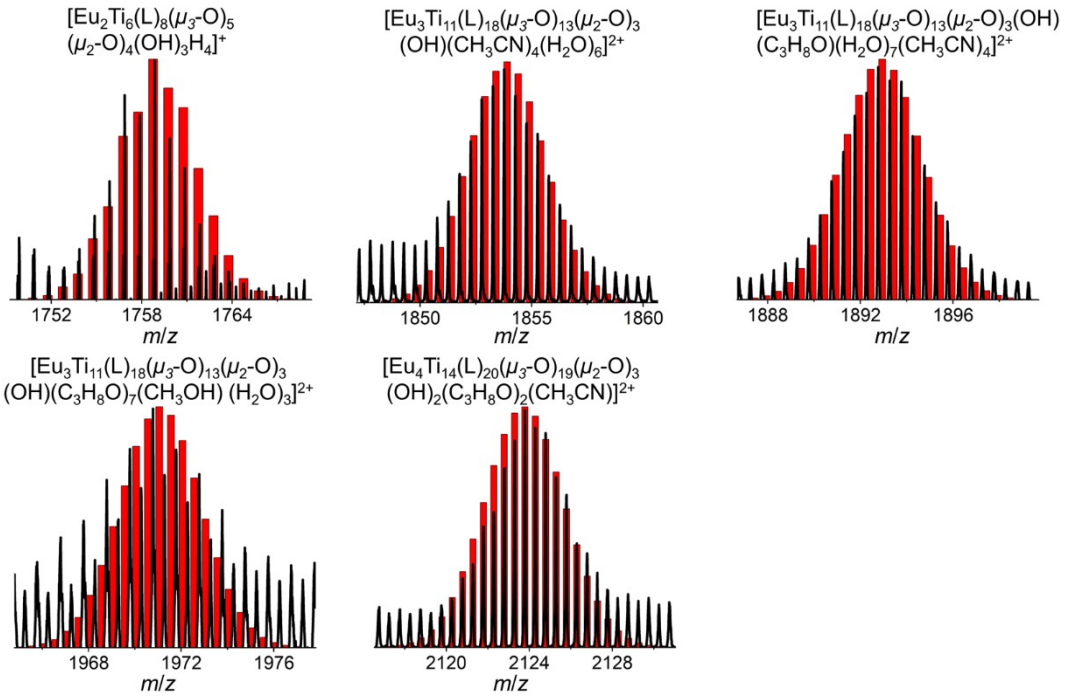

Figure S6. Comparison of experimental (black) and simulated (red) values of the main molecular ion peak of Eu_4Ti_{14} by time-dependent HRESI-MS.

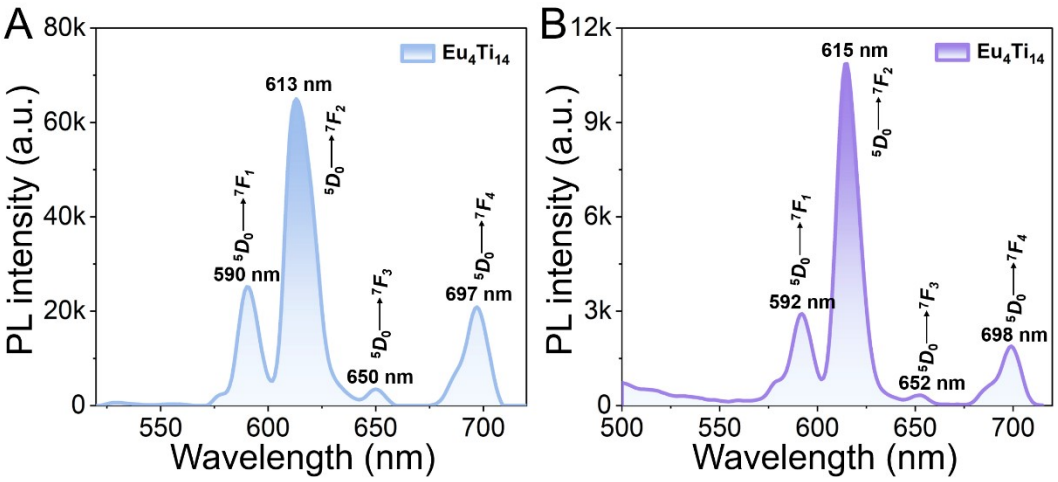

Figure S7. (A) Solid-state emission spectrum of Eu_4Ti_{14} under 395 nm excitation; (B) Emission spectrum of Eu_4Ti_{14} dissolved in DMSO under 395 nm excitation.

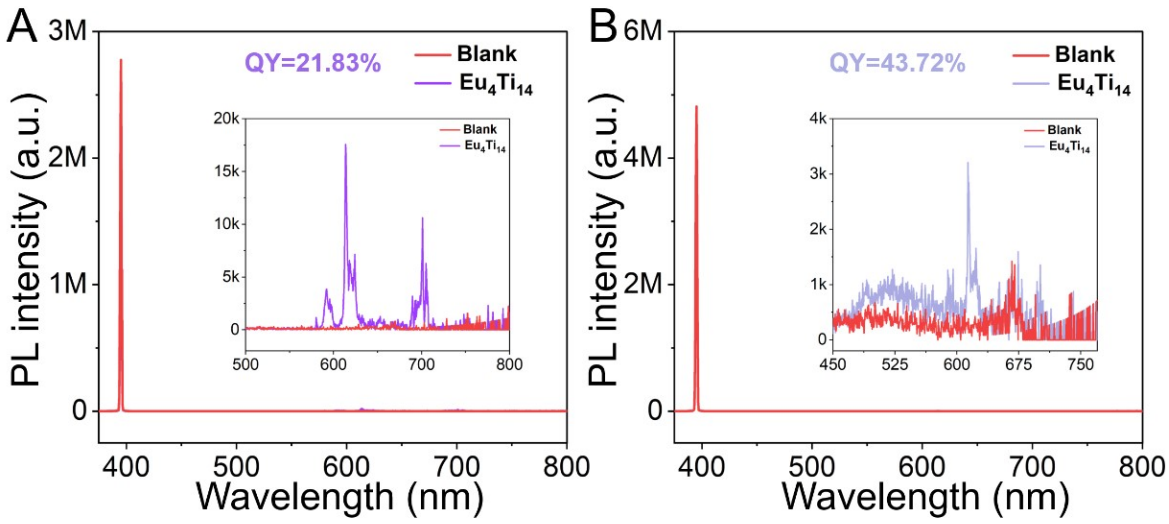

Figure S8. (A) Quantum yield of solid Eu_4Ti_{14}; (B) Quantum yield of Eu_4Ti_{14} dispersed in DMSO solution.

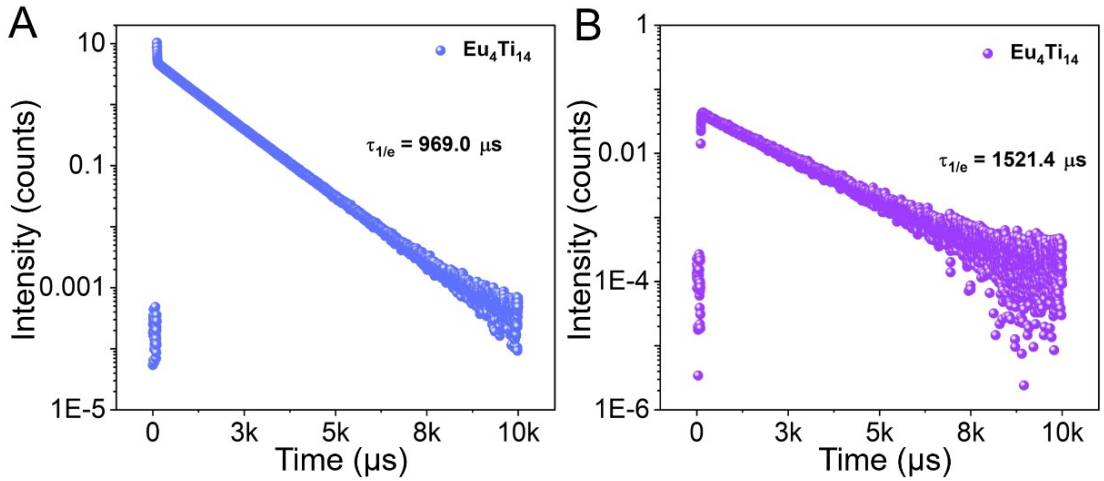

Figure S9. (A) Decay curve of the $^5D_0$ energy level in solid Eu_4Ti_{14}; (B) Decay curve of the $^5D_0$ energy level in Eu_4Ti_{14} in DMSO solution.

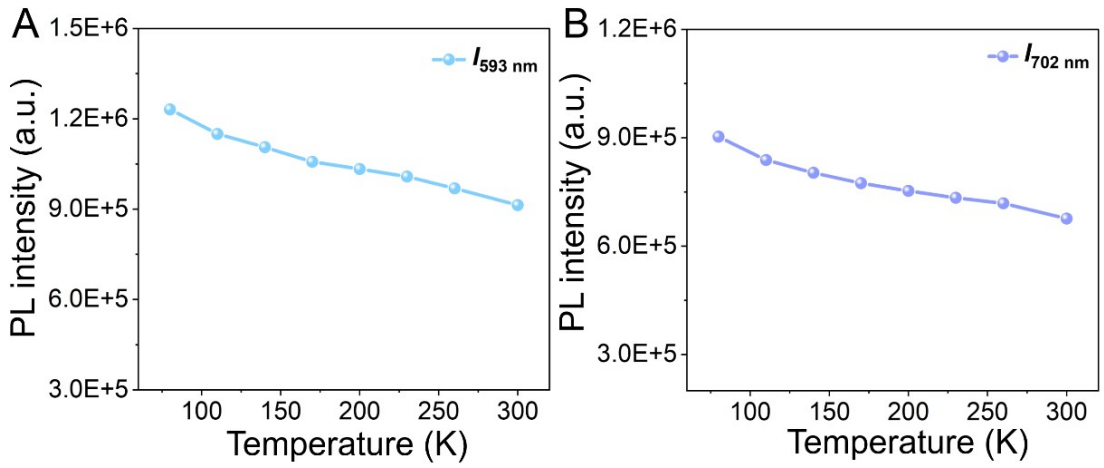

Figure S10. (A) Relationship between the emission intensity at 593 nm and temperature of Eu_4Ti_{14} at 80~300 K; (B) Relationship between the emission intensity at 702 nm and temperature of Eu_4Ti_{14} at 80~300 K.

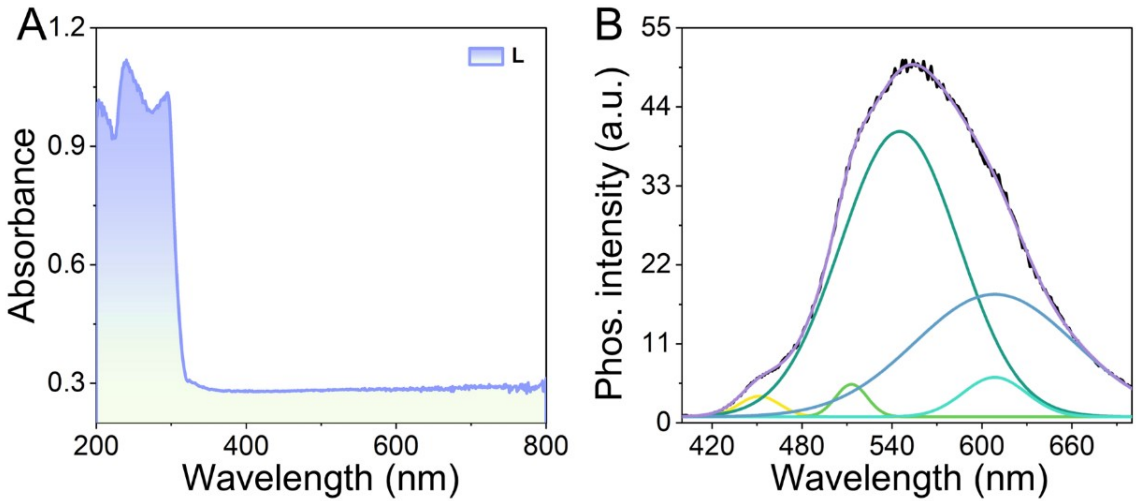

Figure S11. (A) UV-Vis absorption spectrum of the ligand; (B) Phosphorescence spectrum of Gd_4Ti_{14} at low temperature (77 K).

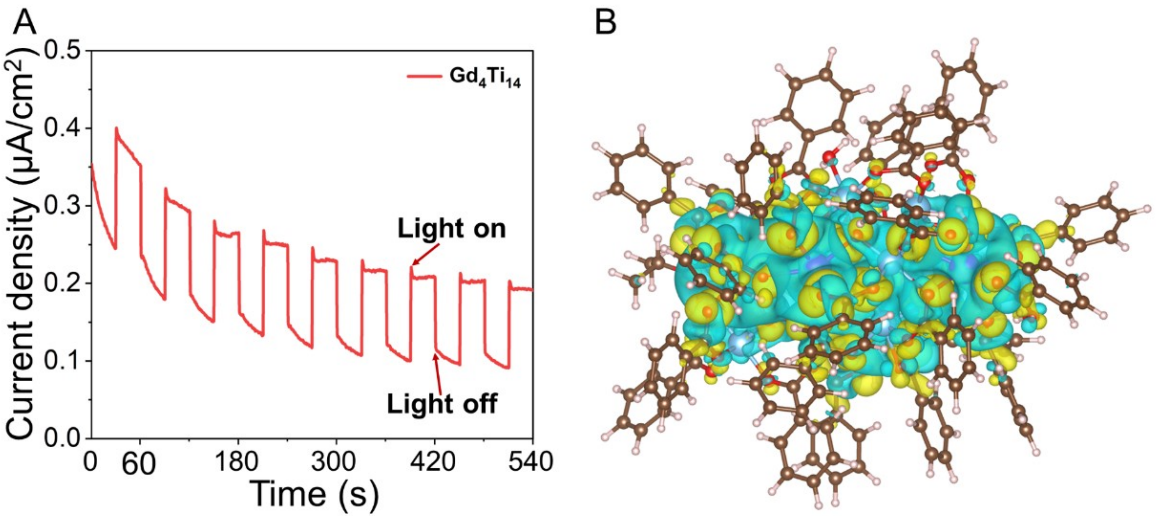

Figure S12. (A) Photocurrent response of Gd_4Ti_{14} under illumination; (B) Electron cloud distribution of Gd_4Ti_{14}.

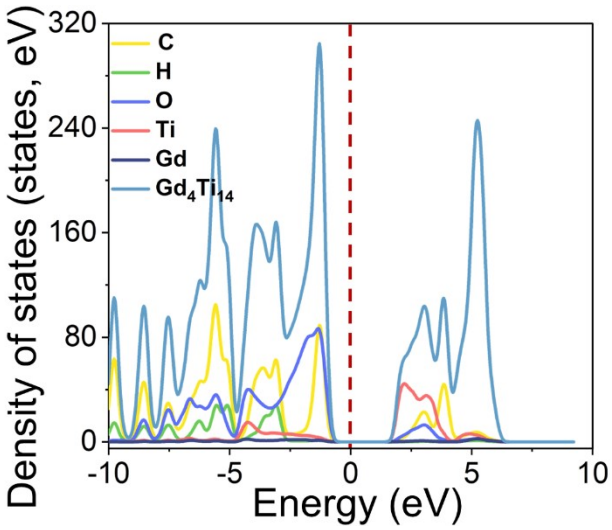

Figure S13. TDOS and PDOS of individual atoms for Gd_4Ti_{14} (the position of the Fermi level is indicated by a red dashed line at 0 eV).

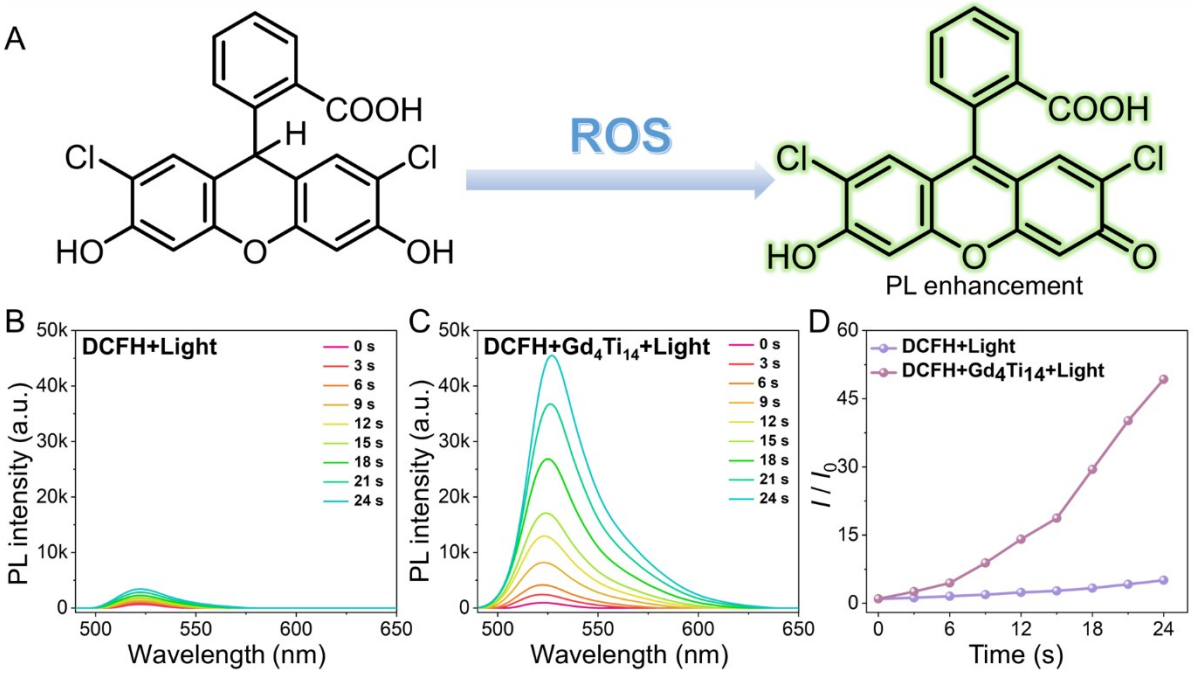

Figure S14. (A) ROS detection mechanism of DCFH; (B) Changes in the PL spectrum of DCFH under light irradiation (60 mW/cm^2); (C) Changes in the PL spectrum of DCFH under light irradiation (60 mW/cm^2) in the presence of Gd_4Ti_{14}; (D) ROS generation of Gd_4Ti_{14} under white light irradiation (60 mW/cm^2) observed by DCFH fluorescence enhancement technology.

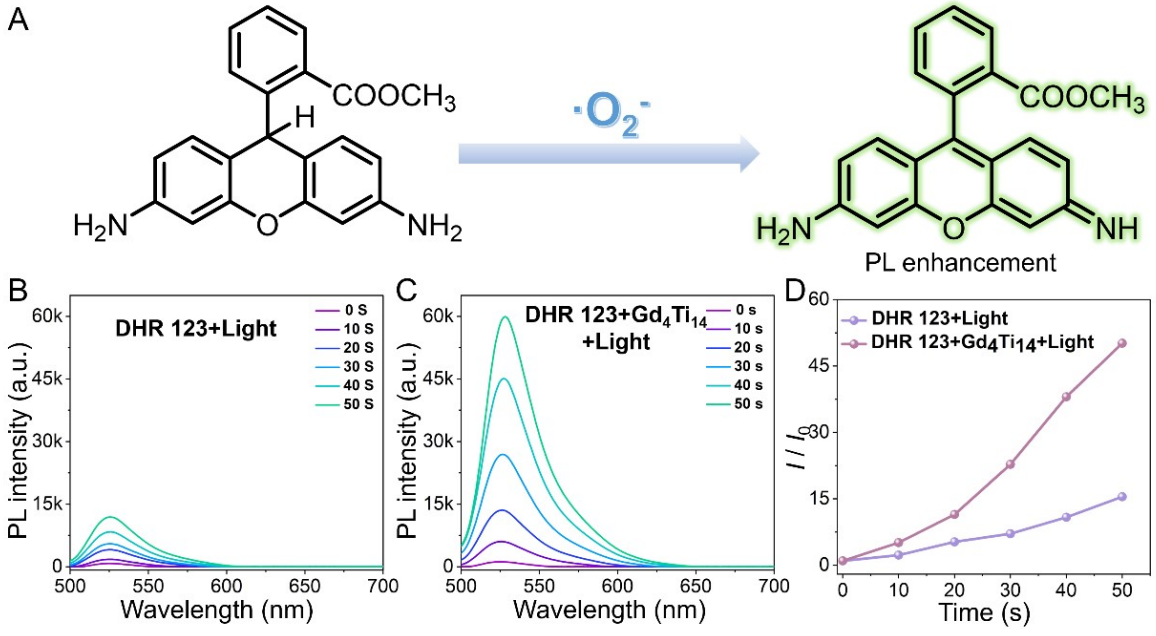

Figure S15. (A) $\cdot O_2^-$ detection mechanism of DHR 123; (B) Changes in the PL spectrum of DHR 123

under illumination (60 mW/cm^2); (C) Changes in the PL spectrum of DHR 123 under illumination (60 mW/cm^2) in the presence of Gd_4Ti_{14}; (D) Monitoring the $\cdot O_2^-$ generation ability of Gd_4Ti_{14} under illumination conditions (60 mW/cm^2) using DHR 123.

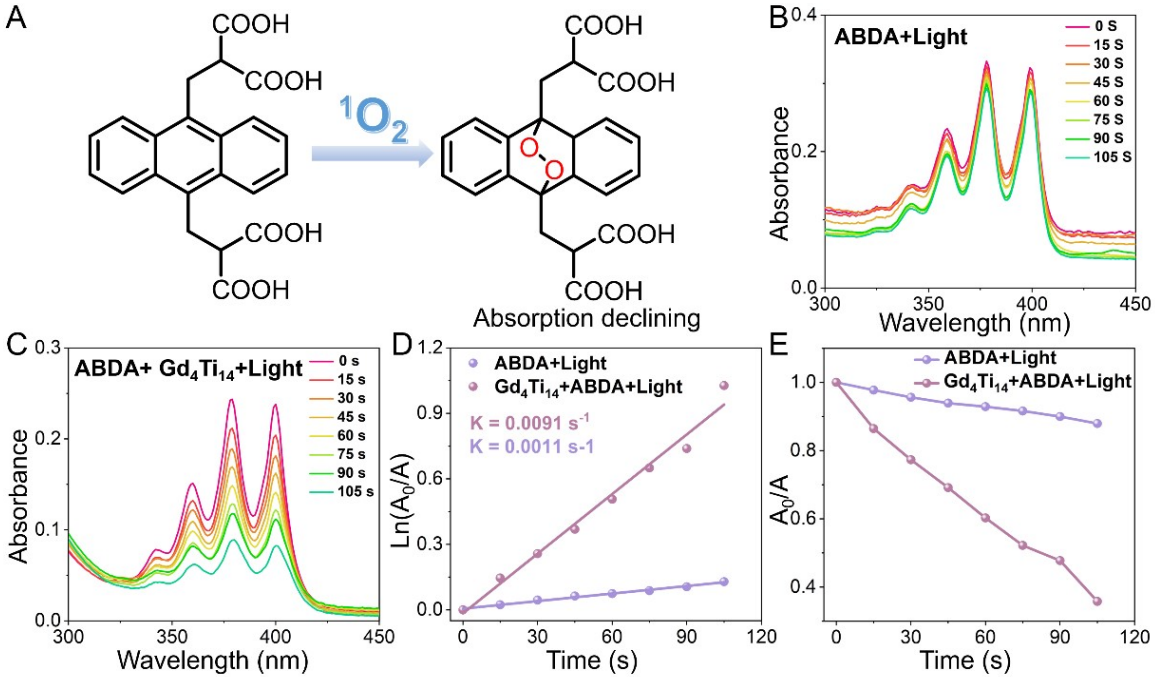

Figure S16. (A) $^1O_2$ detection mechanism of ABDA; (B) UV-vis absorption spectra of ABDA after irradiation at different times (60 mW/cm^2); (C) The absorption spectrum of ABDA changes under different irradiation times (60 mW/cm^2) in the presence of Gd_4Ti1_4; (D and E) The $^1O_2$ generation ability of Gd_4Ti_{14} under light conditions (60 mW/cm^2) was monitored using ABDA.

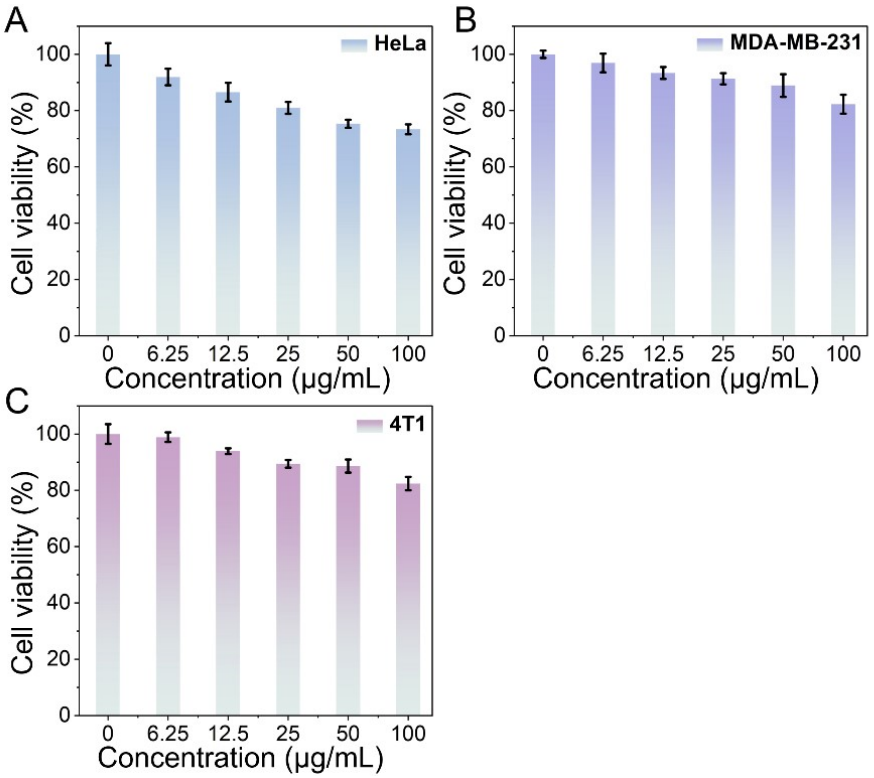

Figure S17. Inhibitory effects of different concentrations of Eu_4Ti_{14} on the growth of (A) HeLa, (B) MDA-MB-231 and (C) 4T1 cells.

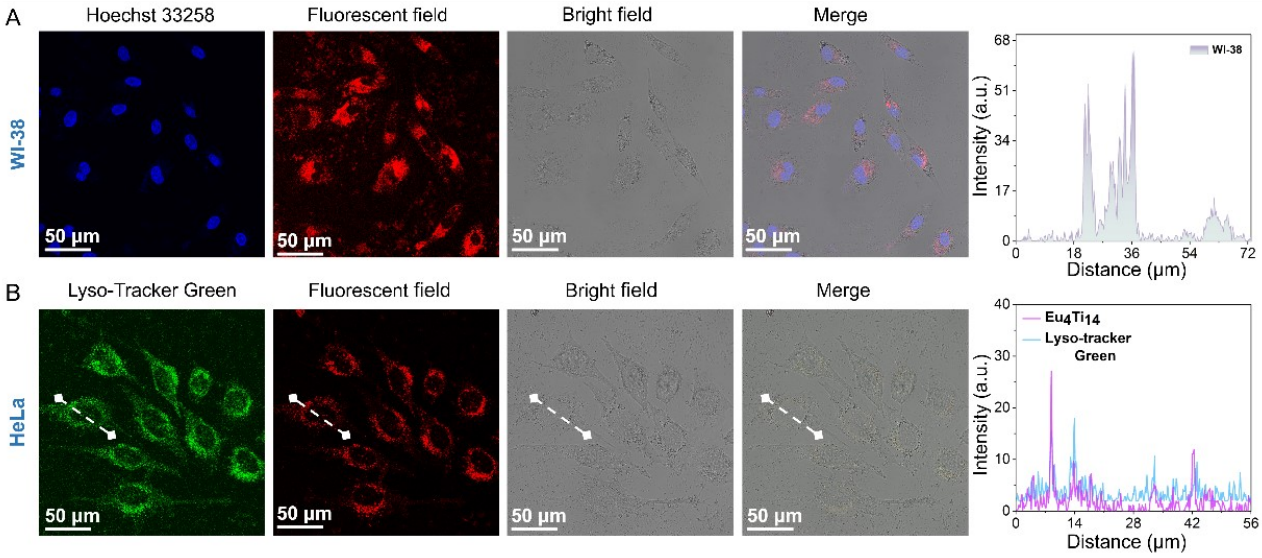

Figure S18. (A) CLSM images and quantitative analysis of fluorescence intensity after co-incubation of Eu_4Ti_{14} with WI-38 cells; (B) CLSM images of Eu_4Ti_{14} and LysoTracker Green in lysosomes of HeLa cells, respectively; quantitative analysis of fluorescence intensity of Eu_4Ti_{14} and LysoTracker Green in

HeLa cells.

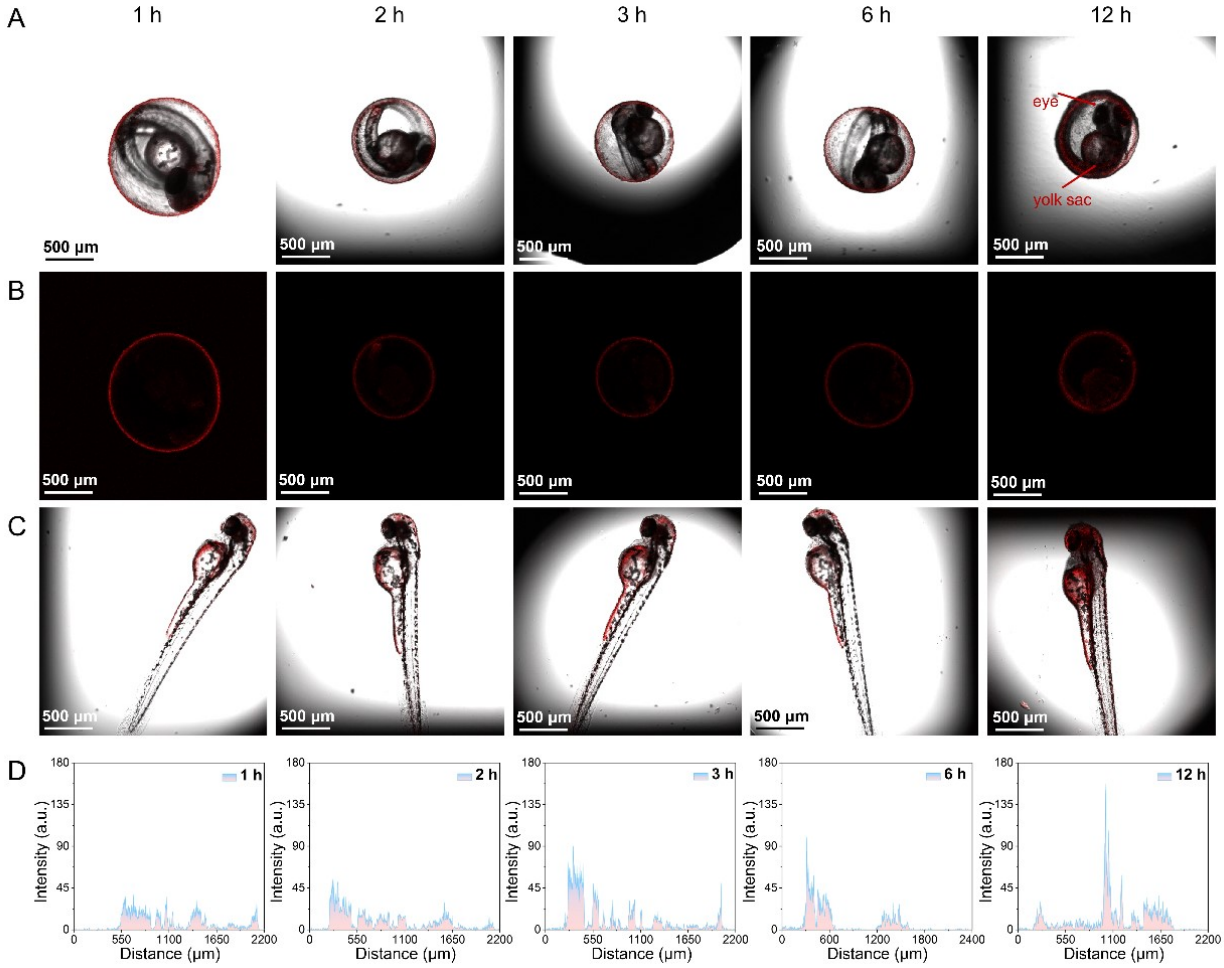

Figure S19. (A and B) CLSM images of Zebrafish embryos co-incubated with Eu_4Ti_{14} for 1, 2, 3, 6, and 12 h; (C) CLSM images of Zebrafish larvae co-incubated with Eu_4Ti_{14} for 1, 2, 3, 6, and 12 h; (D) Quantitative analysis of fluorescence intensity of Zebrafish larvae co-incubated with Eu_4Ti_{14} for 1, 2, 3, 6, and 12 h.

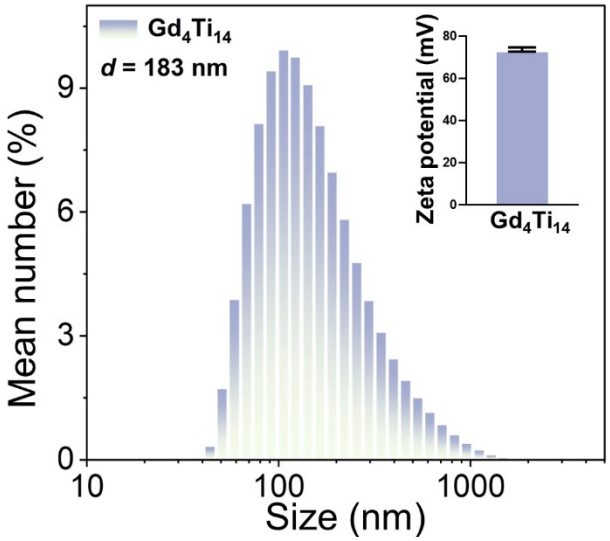

Figure S20. DLS results and Zeta Potential of Gd_4Ti_{14}.

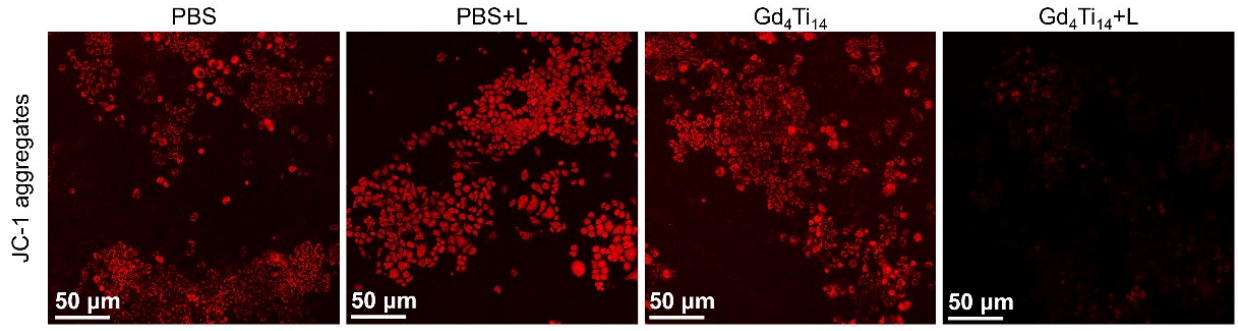

Figure S21. JC-1 staining was used to monitor the changes of mitochondrial membrane potential in different experimental groups.

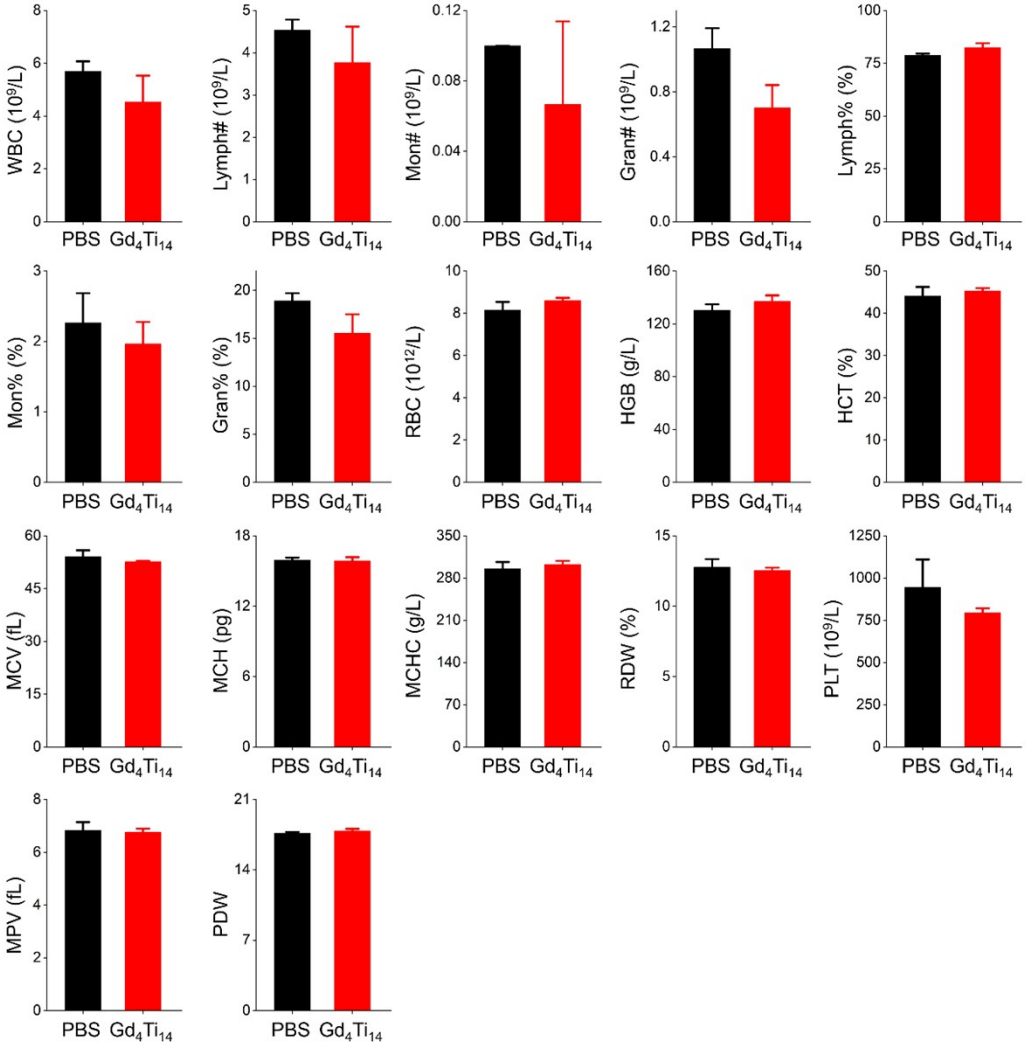

Figure S22. Healthy mice were intravenously injected with PBS or Gd_4Ti_{14} (100 μg/mL, 50 μL) for 24 hours before routine blood analysis (data are expressed as mean ± SD, n = 3, no significant differences).

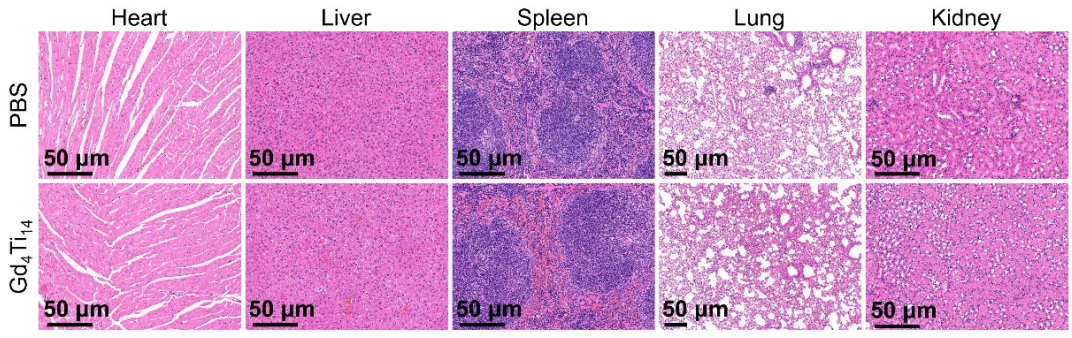

Figure S23. H&E staining results of important organ sections of healthy mice intravenously injected

with PBS or Gd_4Ti_{14} (100 μg/mL, 50 μL).

References

1. S. Wang, H.-C. Su, L. Yu, X.-W. Zhao, L.-W. Qian, Q.-Y. Zhu and J. Dai, Fluorescence and energy transfer properties of heterometallic lanthanide-titanium oxo clusters coordinated with anthracenecarboxylate ligands, *Dalt. Trans.*, 2015, **44**, 1882-1888.
2. D.-F. Lu, Z.-F. Hong, J. Xie, X.-J. Kong, L.-S. Long and L.-S. Zheng, High-Nuclearity Lanthanide-Titanium Oxo Clusters as Luminescent Molecular Thermometers with High Quantum Yields, *Inorg. Chem.*, 2017, **56**, 12186-12192.
3. W. Luo, J.-L. Hou, D.-H. Zou, L.-N. Cui, Q.-Y. Zhu and J. Dai, Lanthanide-titanium-oxalate clusters and their degradation products, photocurrent response and photocatalytic behaviours, *New J. Chem.*, 2018, **42**, 11629-11634.
4. H. Zheng, M. Du, S. Lin, Z. Tang, X. Kong, L. Long and L. Zheng, Assembly of a Wheel-Like $Eu_{24}Ti_8$ Cluster under the Guidance of High-Resolution Electrospray Ionization Mass Spectrometry, *Angew. Chem. Int. Ed.*, 2018, **57**, 10976-10979.
5. R. Chen, Z.-F. Hong, Y.-R. Zhao, H. Zheng, G.-J. Li, Q.-C. Zhang, X.-J. Kong, L.-S. Long and L.-S. Zheng, Ligand-Dependent Luminescence Properties of Lanthanide-Titanium Oxo Clusters, *Inorg. Chem.*, 2019, **58**, 15008-15012.
6. Y.-R. Zhao, H. Zheng, L.-Q. Chen, H.-J. Chen, X.-J. Kong, L.-S. Long and L.-S. Zheng, The Effect on the Luminescent Properties in Lanthanide-Titanium OXO Clusters, *Inorg. Chem.*, 2019, **58**, 10078-10083.
7. W. Luo, X.-P. Shu, P.-Y. Liu, S.-K. Yu, Q.-Y. Zhu and J. Dai, Lanthanide-titanium oxo-clusters, new precursors of multifunctional colloids for effective imaging and photodynamic therapy, *J. Mol. Liq.*, 2020, **317**, 113946.
8. H. Zheng, Y.-K. Deng, M.-Y. Ye, Q.-F. Xu, X.-J. Kong, L.-S. Long and L.-S. Zheng, Lanthanide-Titanium Oxo Clusters as the Luminescence Sensor for Nitrobenzene Detection, *Inorg. Chem.*, 2020, **59**, 12404-12409.
9. K. Zhang and S.-W. Du, Studies of high-nuclearity lanthanide-titanium oxo clusters: Structure and properties, *Inorg. Chim. Acta*, 2021, **528**, 120621.
10. W.-D. Liu, G.-J. Li, H. Xu, Y.-K. Deng, M.-H. Du, L.-S. Long, L.-S. Zheng and X.-J. Kong, Circularly polarized luminescence and performance modulation of chiral europium-titanium (Eu_2Ti_4)-oxo clusters, *Chem. Commun.*, 2023, **59**, 346-349.
11. F. Meng, W.-D. Liu, G.-J. Li, J. Deng and X.-J. Kong, Synthesis, Structure and Luminescence Characterizations of Pyramid-like Lanthanide-Titanium-Oxo Clusters $EuTi_9$ and $TbTi_9$, *Inorg. Chem. Commun.*, 2022, **141**, 109565.
12. W.-D. Liu, G.-J. Li, H. Xu, M.-H. Du, L.-S. Long, L.-S. Zheng and X.-J. Kong, Photoluminescence of Lanthanide-Titanium-Oxo Clusters Eu_9Ti_2 and Tb_9Ti_2 Based on a *β*-Diketone Ligand, *Inorg. Chem.*, 2022, **61**, 9849-9854.
13. M. Du, S. Xu, G. Li, H. Xu, Y. Lin, W. Liu, L. Long, L. Zheng and X. Kong, Modification of Multi-Component Building Blocks for Assembling Giant Chiral Lanthanide-Titanium Molecular Rings, *Angew. Chem. Int. Ed.*, 2022, **61**, e202116296.
14. R. Chen, C.-L. Chen, H. Zhang, Z.-H. Wang, F.-L. Sun, M.-H. Du, G.-L. Zhuang, C. Wang, L.-S. Long, L.-S. Zheng and X.-J. Kong, Molecular solid solution of lanthanide-titanium-oxo clusters with enhanced photocatalytic hydrogen evolution, *Sci. China Chem.*, 2024, **67**, 529-535.
15. W. Liu, H. Xu, C. Li, L. Long, L. Zheng and X. Kong, Magneto-optical response and luminescence

properties of lanthanide-titanium-oxo clusters Eu_2Ti_7 and Sm_2Ti_7, *Inorg. Chem. Front.*, 2025, **12**, 253-260.

16. 1 X. Yan, M. Zhao, F. Jiang, H. Zhu, W. Dong, S. He, J. Xia, M. Hong, Z. Wu and X. Bai, Ligand rigidity-mediated coordination symmetry engineering in lanthanide-titanium nanoclusters achieves > 90% photoluminescence quantum yield, *J. Rare Earths*, 2025, **43**, 1590-1600.
17. F. Jiang, S. He, Y. Ji, J. Yin, Y. Cong, W. Dong, X. Li, Y. Zhang, Z. Wu and X. Bai, Suppression of Photoexcited Small Polarons-Mediated Energy Transfer to Boost Photoluminescence of Lanthanide-Titanium Nanoclusters, *Nano Lett.*, 2025, **25**, 1199-1206.